



# Modulating the electronic structures derived by neighbouring hetero-diatom FeCoN<sub>6</sub>-Gra for prominent electrocatalysis of arsenious acid

Yong-Yu Li<sup>a,b</sup>, Zong-Yin Song<sup>b,c</sup>, Zhi-Wei Gao<sup>b,c</sup>, Xiang-Yu Xiao<sup>b,c</sup>, Yong-Huan Zhao<sup>b,c</sup>,  
Pei-Hua Li<sup>b,c,\*</sup>, Xing-Jiu Huang<sup>b,c,\*</sup>, Wen-Qing Liu<sup>a,d,\*\*</sup>

<sup>a</sup> School of Environmental Science and Engineering, Tianjin University, Tianjin 300350, PR China

<sup>b</sup> Key Laboratory of Environmental Optics and Technology, And Environmental Materials and Pollution Control Laboratory, Institute of Solid State Physics, HFIPS, Chinese Academy of Sciences, Hefei 230031, PR China

<sup>c</sup> Department of Materials Science and Engineering, University of Science and Technology of China, Hefei 230026, PR China

<sup>d</sup> Anhui Institute of Optics and Fine Mechanics, HFIPS, Chinese Academy of Sciences, Hefei 230031, PR China

## ARTICLE INFO

### Keywords:

Dual active sites  
Rearrangement of electrons  
Site distance effect  
Driving effect  
Electrocatalytic reduction of As(III)

## ABSTRACT

Single atom catalysts (SACs) have been widely studied in the field of electrocatalytic reduction, but in the complex multi-step proton-electron reactions, the metal active site is easy to be weakened or even poisoned. Therefore, how to improve the adsorption-desorption capacity and rapid surface reaction to obtain superior electrocatalytic performance remains a great challenge. We indicate the electron synergism of neighbouring Fe and Co diatoms on graphene (FeCoN<sub>6</sub>-Gra) to promote the electrocatalytic reduction of arsenious acid (As(III)), which is superior to single-atomic catalysts containing only Fe or Co. It is found that the new electron allocation mechanism associated with the injection of Co is beneficial to trigger the two-site adsorption and effectively regulate electron transport between surface sites and As(III). Moreover, the dynamic migration of As(III) driven by Co atom during the reduction process is emphasized, which contributes to break the As-O bond, thus achieving efficient catalysis of the diatomic model.

## 1. Introduction

Arsenic is a highly toxic and carcinogenic pollutant, especially trivalent H<sub>3</sub>AsO<sub>3</sub> [1–3]. It is estimated that at least 200 million people worldwide are threatened by excessive content of arsenic in groundwater and natural water [4,5]. Therefore, the realization of trace detection of H<sub>3</sub>AsO<sub>3</sub> is an urgent demand for human health and environmental safety. In the field of electrocatalysis, the redox reaction of As(III) is extremely difficult to occur due to the high reaction barrier required to overcome the breaking of the three As-O bonds. In recent years, various sensing strategies have been explored for prominent electrocatalysis of As(III) [6,7]. Li et al. introduced ionic valence state cycle engineering into electroanalysis, and electron transfer between surface-activated Fe(II)/Fe(III) promoted efficient catalysis of As(III) [8]. Chen et al. constructed electron-rich sites for selective catalytic

detection of As(III) from vacancy engineering and doping engineering [9]. Huang's team found that the reaction energy barrier of the rate-determining step for As(III) reduction affects the deposition of As(0), which interferes with the accuracy of the As(III) response signal [10]. Obviously, the exploration of the interaction mechanism between the active site of the catalyst and the target analyte is conducive to the efficient electrical analysis of As(III), which mainly involves the process of increasing the reaction rate and changing the rate-determining step of the redox reaction, so that researchers can more scientifically select or construct catalytic materials [6,11]. Hence, it remains challenging to design catalysts that reveal the mechanism of surface electron interaction at the atomic scale while ensuring that the requirements for efficient adsorption/desorption and rapid surface reactions are maximized.

As we all know, excellent electrocatalytic performance depends on the surface properties of the catalyst, which means that the atoms inside

\* Corresponding authors at: Key Laboratory of Environmental Optics and Technology, And Environmental Materials and Pollution Control Laboratory, Institute of Solid State Physics, HFIPS, Chinese Academy of Sciences, Hefei 230031, PR China.

\*\* Corresponding author at: School of Environmental Science and Engineering, Tianjin University, Tianjin 300350, PR China.

E-mail addresses: [peihuali@issp.ac.cn](mailto:peihuali@issp.ac.cn) (P.-H. Li), [xingjiuhuang@iim.ac.cn](mailto:xingjiuhuang@iim.ac.cn) (X.-J. Huang), [wqliu@aiomf.ac.cn](mailto:wqliu@aiomf.ac.cn) (W.-Q. Liu).

<https://doi.org/10.1016/j.apcatb.2023.122851>

Received 9 December 2022; Received in revised form 19 April 2023; Accepted 3 May 2023

Available online 9 May 2023

0926-3373/© 2023 Published by Elsevier B.V.

the particles or clusters cannot be used efficiently [12,13]. Single-atom catalysts (SACs) based on carbon materials have highly active coordination environment and high atomic utilization efficiency, as well as explicit active sites [14–16]. It is commendable that SACs do not have complicated surface defects, and unlike traditional materials which inevitably involve a variety of interference sites such as crystal surfaces and vertices [17,18]. Clearly, SACs provide an ideal model and research platform for revealing the detection mechanism of specific heavy metal pollutants in the process of electrical analysis [19–22]. On the other hand, dispersed metal atom and their adjacent coordination environments play a crucial role in determining activity, selectivity, and stability [23]. However, it should not be ignored that SACs have low load and single site [24,25]. Especially in the multi-step proton-electron transfer process, it is easy to cause metal center poisoning and weak performance [26–28]. To get rid of this dilemma, researchers carefully regulate the interaction between the catalytic sites and the carrier coordination environment to optimize the molecular adsorption strength or modify the binding energy of the intermediate [29,30]. Studies have shown that the catalytic activity of SACs can be significantly affected by the introduction of another metal atom into the coordination environment [31,32]. In addition, different binding strengths can be customized to make up for the deficiency of single-atom catalysts by changing the combination of two metals in dual-atom catalysts (DACs) [33–35]. Extensive theoretical data also verify that the unique electronic synergy between two adjacent metal active sites in DACs can effectively change the overall electronic arrangement of atom pairs [36–38]. Yi et al. confirmed that Cu-Co heteronuclear diatoms are conducive to reducing the energy barrier of key intermediates and accelerating the adsorption-desorption performance [39]. Moreover, Li's team specifically regulated the interatomic distance to activate the two-site adsorption mode, which significantly improved the kinetics of the catalytic reaction [40]. Chen et al. induced electron transfer by inserting single atoms, which significantly improved the catalytic activity [41]. Generally, it was indicated that the elaborate regulation of the coordination environment of the single atom catalytic center plays a crucial role in achieving high catalytic activity, especially for catalytic reactions with complex reductions such as As(III) [42,43].

Here, we investigated the synergistic effect of adjacent metal pairs by placing dispersed Co atom around Fe single atom in nitrogen-doped graphene (FeCoN<sub>6</sub>-Gra) and illustrated the impact of Co atom on dynamic migration during the reduction of As(III) at Fe sites. FeCoN<sub>6</sub>-Gra catalyst showed excellent sensitivity and selectivity for As(III), superior to SACs containing only Fe or Co sites. Based on the experimental results, the reliable structure of the FeCoN<sub>6</sub>-Gra model is established by DFT calculation. The enhanced catalytic activity results from the overall new electron allocation mechanism of FeCo atoms. The bimetallic site distance effect facilitates electron transfer by modifying adjacent Co atoms. And Co atoms simultaneously drive the migration of As species to the bridge site of atomic pairs, which is conducive to break the As-O bond, resulting in the efficient catalysis of the diatomic model.

## 2. Experiment section

### 2.1. Synthesis of FeCoN<sub>6</sub>-Gra, FeN<sub>4</sub>-Gra, and CoN<sub>4</sub>-Gra

Further improving on our previous study [44], diatomic FeCoN<sub>6</sub>-Gra was prepared by an in-situ pyrolysis strategy. Firstly, 0.25 g of glucose and 5 g of DCD were dissolved in 200 mL of deionized water, then 10 mL of a mixture of Fe(NO<sub>3</sub>)<sub>3</sub>·9 H<sub>2</sub>O solution (1.25 mM) and Cu(NO<sub>3</sub>)<sub>2</sub>·6 H<sub>2</sub>O solution (1.25 mM) was slowly added solution. Subsequently, the resulting solution was further stirred and heated at 80 °C until the deionized water evaporated. The resulting product was finely ground into powder with a mortar. Afterwards, the powder collected as a precursor was placed in a covered crucible and pyrolyzed in Ar at a rate of 3 °C min<sup>-1</sup> for 2 h at different temperatures. In addition, the synthesis steps of single-atom Fe (FeN<sub>4</sub>-Gra) and Co (CoN<sub>4</sub>-Gra) are similar to the

above, except that the corresponding metal sources used are Fe(NO<sub>3</sub>)<sub>3</sub>·9 H<sub>2</sub>O solution (5 mL) and Cu(NO<sub>3</sub>)<sub>2</sub>·6 H<sub>2</sub>O solution (5 mL).

### 2.2. Electrochemical tests

The traditional three-electrode system was adopted, with the screen-printed carbon electrode (SPCE, diameter 3 mm) as the working electrode, platinum wire as the auxiliary electrode, and Ag/AgCl (saturated KCl) as the reference electrode. The square-wave anodic stripping voltammetry (SWASV) was used to determine the detection of As(III) on the modified electrode in 0.1 M acetic acid-sodium acetate solution. The applied voltage is swept from −1–0.8 V with a frequency of 15 Hz and an amplitude of 0.025 V. In addition, 1.0 V desorption was applied to the working electrode for 180 s to remove the remaining As species after each measurement. All electrochemical data were statistically analyzed, and error bars corresponding to the standard deviations of the three independent measurements were given.

## 3. Results and discussion

### 3.1. Morphology and structure characterization of CoN<sub>4</sub>-Gra, FeN<sub>4</sub>-Gra, and FeCoN<sub>6</sub>-Gra

At the optimum temperature of 900 °C (Fig. S2), the preparation process of ultra-thin two-dimensional (2D) dual-site FeCo catalyst shown in Fig. S1 was obtained based on one-step calcination followed by complete mixing. Fig. S3a, Fig. S3b, and Fig. 1a correspond to scanning electron microscopy (SEM), transmission electron microscopy (TEM) and high-angle annular dark-field scanning transmission electron microscopy (HAADF-STEM) of FeCoN<sub>6</sub>-Gra, respectively. It is easy to see that there are a lot of wrinkles on the thin graphene, and no large particles or clusters are observed on closer inspection. Combined with energy-dispersive spectrometry (EDS, Fig. S3c), element distribution diagram of FeCoN<sub>6</sub>-Gra (Fig. 1b) shows that Fe and Co elements are uniformly embedded in graphene (without impurity elements), which fits the outline of the catalyst in Fig. 1a. Further magnification of the HAADF-STEM image in Fig. 1c shows that FeCoN<sub>6</sub>-Gra has both single and double single-atom (highlighted by red circles) at thinner locations. According to the analysis of the intensity profiles (Fig. 1d) of region A and B, the distance between the two adjacent metal atoms is about 2.35 Å. Meanwhile, electron energy loss spectroscopy (EELS, Fig. 1e) collected in the highlighted region containing the double spots further verified that Fe and Co atoms are adjacent at the atomic level, revealing the existence of Fe-Co double sites [45]. For comparison, the catalysts of FeN<sub>4</sub>-Gra and CoN<sub>4</sub>-Gra were also characterized. According to SEM (Fig. S4a and Fig. S5a) and TEM (Fig. S4b and Fig. S5b), it can be concluded that both FeN<sub>4</sub>-Gra and CoN<sub>4</sub>-Gra have almost no difference in morphology with FeCoN<sub>6</sub>-Gra, which are characteristics of 2D graphene containing a large number of folds. Combined with EDS (Fig. S4c and Fig. S5c) and elemental mapping (Fig. S4d and Fig. S5d), Fe/Co was evenly incorporated into the graphene. As observed from the HAADF-STEM in Fig. S4e and Fig. S5e, there are no metal nanoparticles or clusters in the entire N-doped graphene carrier. At sub-angstroms resolution, many sparsely distributed bright spots were observed (Fig. S4f and Fig. S5f), indicating that there are no tiny clusters but isolated Fe or Co atoms. The X-ray diffraction (XRD) pattern also revealed no large particles in the bulk phase [46,47]. No diffraction peaks of metal nanoparticles are observed in Fig. S6, except for the broad diffraction peaks around 25° and 44° correspond to (002) and (101) planes of graphite carbon [48]. As illustrated in Fig. S7, the specific surface areas of FeN<sub>4</sub>-Gra, CoN<sub>4</sub>-Gra, and FeCoN<sub>6</sub>-Gra were 335.83, 216.21, and 283.65 m<sup>2</sup>·g<sup>-1</sup>, respectively. The illustrations showed that the aperture size of the three catalysts were mainly in the range of 20 ~ 100 nm. The Raman results in Fig. S8 also indicate that the properties of the samples are basically the same except for the information related to the active site structure [49]. Besides, the load amount of Fe atoms in

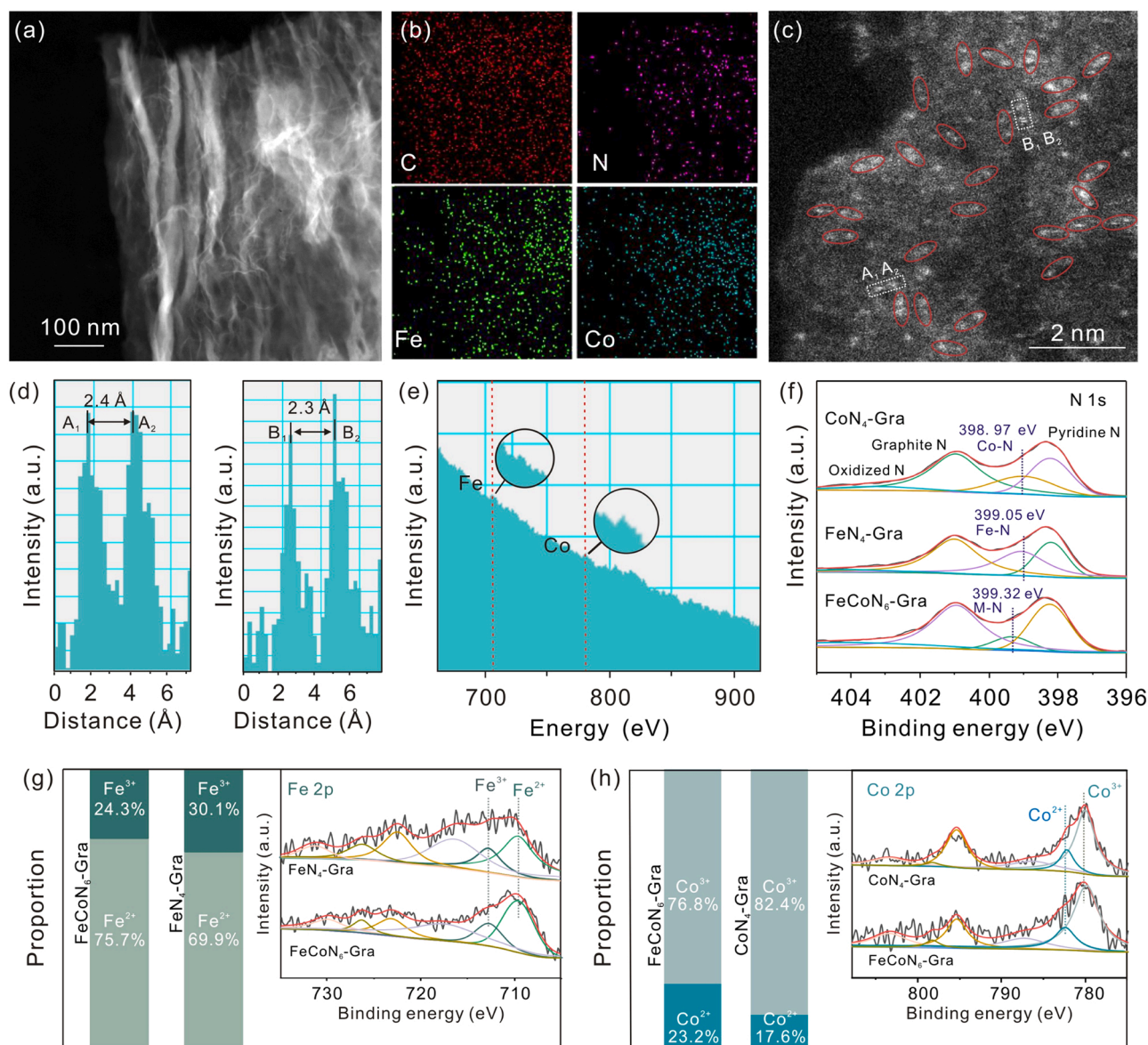


**Fig. 1.** (a) HAADF-STEM image of FeCoN<sub>6</sub>-Gra. (b) Element mapping of C (red), N (purple), Fe (green), and Co (blue). (c) High magnification of HAADF-STEM at a thin position of FeCoN<sub>6</sub>-Gra, pairs of atoms are circled in red. (d) The corresponding intensity profiles of region A and B. (e) Point scan EELS spectra of FeCoN<sub>6</sub>-Gra. (f) High-resolution XPS of N 1s in CoN<sub>4</sub>-Gra, FeN<sub>4</sub>-Gra, and FeCoN<sub>6</sub>-Gra, (M is Fe or Co). (g) Bar chart of the ratio of Fe (II) to Fe (III), the insets are Fe 2p in FeN<sub>4</sub>-Gra and FeCoN<sub>6</sub>-Gra. (h) Bar chart of Co (II) and Co (III) ratios, the illustrations are the high-resolution XPS of Co 2p in CoN<sub>4</sub>-Gra and FeCoN<sub>6</sub>-Gra.

FeN<sub>4</sub>-Gra is 1.09 wt% determined by inductively coupled plasma emission spectroscopy (ICP-OES), which is close to the load amount of Co atoms in CoN<sub>4</sub>-Gra (1.11 wt%). The load amount of Fe and Co metal atoms in FeCoN<sub>6</sub>-Gra are 1.24 wt% and 1.17 wt%, respectively. (Table S1).

For further determination of chemical composition and electronic state, X-ray photoelectron spectroscopy (XPS) was performed on FeCoN<sub>6</sub>-Gra, FeN<sub>4</sub>-Gra, and CoN<sub>4</sub>-Gra. Fig. 1f is the comparison of N 1s spectra of the catalysts. Except for pyridinic N (~ 398.1 eV), graphitic N (~ 401 eV), and oxidized N (~ 403 eV) [50], there is a peak around 399 eV corresponding to M-N bond (M is Fe or Co). This means that the incorporated Fe/Co atoms are fixed in the carbon carrier by bonding with the N atom. Moreover, compared with FeN<sub>4</sub>-Gra and CoN<sub>4</sub>-Gra, a shift of 0.3 eV to the high binding energy implies that N atoms lost more electrons in FeCoN<sub>6</sub>-Gra. From Fig. 1g and Fig. 1h, it can be made clear first that the presence of satellite peaks excludes zero-valent elements [51]. Secondly, both Fe and Co exhibit very distinct valence states, in which Co tends to be Co<sup>3+</sup>, while Fe mainly shows Fe<sup>2+</sup>. Obviously, the

active site of the lower state is conducive to the adsorption of the target to transfer electrons [8,10]. We speculate that the active site of Fe<sup>2+</sup> is more likely to capture more H<sub>3</sub>AsO<sub>3</sub> in the process of pre-concentration, and further bond with As atoms to promote the reduction of As(III). In the following dissociation of As(III), the adjacent Co<sup>3+</sup> atom can effectively regulate the bonding strength of Fe-As, which contributes to the dissociation process. Finally, the comparing results of Fe 2p and Co 2p jointly declare that the electron gain capacity of each metal in FeCoN<sub>6</sub>-Gra is stronger than that of the active site in the homologous single atom catalyst. This means that more electrons are allocated to each atom than to Fe in FeN<sub>4</sub>-Gra or Co in CoN<sub>4</sub>-Gra, because the coordinated N atoms in FeCoN<sub>6</sub>-Gra transfer more electrons to the diatomic. And this new electron allocation mechanism lays a unique advantage for the subsequent adsorption-desorption of As species or intermediates.

To figure out the localized electronic structure and coordination information of the dual-atom centered site configuration, extended X-ray absorption fine structure (EXAFS) and X-ray absorption near edge



spectroscopy (XANES) were used. From the Fe K-edge XANES spectrum in Fig. 2a, it is found that the Fe in single-atom samples was between +2 and +3 valence, and the Fe in FeCoN<sub>6</sub>-Gra was slightly lower than that in FeN<sub>4</sub>-Gra under closer observation. A similar tendency was observed in the Co K-edge XANES spectrum of Fig. 2b. This meant that the dual-atom centered sites in the FeCoN<sub>6</sub>-Gra gained more electrons relative to the cognate single-atom catalyst, which was consistent with the XPS results. The EXAFS Fourier transform (FT) spectrum of the Fe K-edge (K<sup>3</sup>-weighted) in Fig. 2c showed a scattering path corresponding to Fe-N at 1.4 Å without Fe-Fe interactions (without phase correction), indicating that the dispersed Fe atoms were stably anchored in the graphene via N atoms. The fitting results showed that the coordination number of Fe was about 3.7 and the average bond distance is 1.99 Å (Table S2). The fitting results of CoN<sub>4</sub>-Gra (Fig. 2d) showed that Co was fixed by 3.99 coordination N atoms with a bond length of 1.85. Based on the EXAFS spectra of Fe/Co k-edge of FeCoN<sub>6</sub>-Gra (Fig. 2e, Fig. 2f), the significant peak occurred around 1.4 Å, which was assigned to the metal-N scattering path. In particular, the scattering peak around 2.2 Å corresponded to Fe-Co/Fe-Co, implying that the second shell of Fe/Co was a metal atom, whereas FeN<sub>4</sub>-Gra or CoN<sub>4</sub>-Gra had no such signal at the same

location. The fitting results further revealed that both Fe and Co coordinated with about 4 N atoms, with average bond lengths of 1.73 and 1.81 Å, respectively. The scattering peaks in the second shell correspond to Fe-Co/Co-Fe with coordination numbers close to 1. It also proved that the Fe and Co atoms were indeed adjacent to each other, and the spacing was around 2.28 Å. The fitting curve in Fig. S9 fitted well with the original data, indicating the accuracy and reliability of the above analysis results.

### 3.2. Electronic structure of catalysts calculated by DFT

Density functional theory (DFT) can deeply investigate the fundamental principle for catalytic activity, and effectively guide the rational designing or screening of catalysts by elucidating mechanistic insights [52–54]. Based on DFT calculation, the corresponding geometry optimization configurations were shown in Fig. S10, and the obtained structural parameters were in good agreement with the characterized data. We further compared the density of states (DOS) of FeCoN<sub>6</sub>-Gra, homologous monatomic samples, and metallic bulk materials with that of free H<sub>3</sub>AsO<sub>3</sub>, as shown in Fig. 2g. Compared with the metal block, the

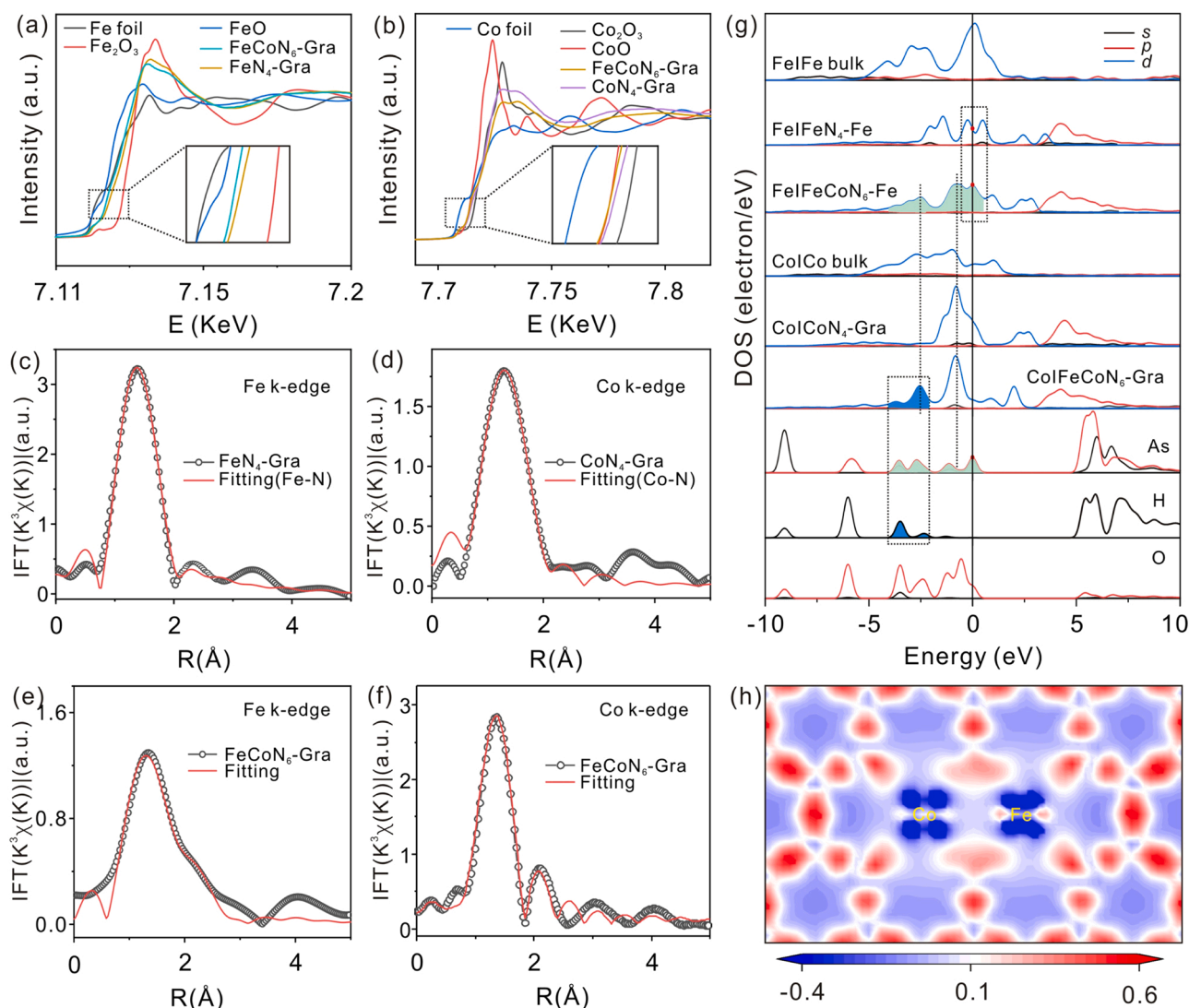


**Fig. 2.** (a) Normalized Fe K-edge XANES spectra of the Fe foil, FeO, Fe<sub>2</sub>O<sub>3</sub>, FeN<sub>4</sub>-Gra, and FeCoN<sub>6</sub>-Gra. (b) Normalized Co K-edge XANES spectra of the Co foil, CoO, Co<sub>2</sub>O<sub>3</sub>, CoN<sub>4</sub>-Gra, and FeCoN<sub>6</sub>-Gra, the inset corresponds to the magnified dashed box area. The EXAFS Fourier transformed (FT) spectra of (c) Fe K-edge and (d) Co K-edge (k<sup>3</sup>-weighted) and their corresponding fitting curves. (e) Fe and (f) Co K-edge EXAFS FT spectra (k<sup>3</sup>-weighted) of FeCoN<sub>6</sub>-Gra and their corresponding fitting. (g) DOS comparison of Fe atom in Fe bulk, FeN<sub>4</sub>-Gra, and FeCoN<sub>6</sub>-Gra, Co atom in Co bulk, CoN<sub>4</sub>-Gra, and FeCoN<sub>6</sub>-Gra, and free H<sub>3</sub>AsO<sub>3</sub>. (h) Charge density difference image of FeCoN<sub>6</sub>-Gra. The blue area represented the loss of electrons, red represented electron accumulation.

electrons at Fermi level of FeN<sub>4</sub>-Gra/CoN<sub>4</sub>-Gra were redistributed. More exciting, the electron distribution of Fe/Co atoms in FeCoN<sub>6</sub>-Gra was further improved. Firstly, it was evident that there was a strong coupling between Fe and Co, especially at  $-1.0$  eV and  $-2.5$  eV, respectively, indicating the existence of electronic interaction. Secondly, the number of Fe electrons on the Fermi level (red dots on Fermi level) was reflected, and the electron distribution of Fe was more consistent with the position of the As(III) level (the green-filled region of  $-4 \sim 0$  eV). But the electron distribution of diatomic Co was more diffuse and matched the atomic energy level of H (blue-filled area). This potential binding tendency laid the foundation for subsequent two-site adsorption. Fig. 2h was a charge density difference slice of FeCoN<sub>6</sub>-Gra, which visually reflected the distribution and transfer of electrons after doping (red represented electron gain and blue was loss). For a better comparison, FeN<sub>4</sub>-Gra and CoN<sub>4</sub>-Gra were treated with the same density gradient as shown in Fig. S11, and FeFeN<sub>6</sub>-Gra and CoCoN<sub>6</sub>-Gra were supplemented. It was worth mentioning that the electron distribution between FeFeN<sub>6</sub>-Gra and CoCoN<sub>6</sub>-Gra was evenly distributed, while the Fe in the asymmetric FeCoN<sub>6</sub>-Gra was more likely to aggregate electrons. This was directly confirmed by the quantitative Mulliken values (Table S3), which further indicated that Fe was more likely to be the adsorption site in the FeCo two-site configuration.

### 3.3. Evaluation on the electroanalytical performance of As(III)

Firstly, the impedance of FeCoN<sub>6</sub>-Gra, FeN<sub>4</sub>-Gra, and CoN<sub>4</sub>-Gra modified electrodes was evaluated (Fig. S12). The results showed that FeCoN<sub>6</sub>-Gra modified SPCE was the best, followed by FeN<sub>4</sub>-Gra and CoN<sub>4</sub>-Gra. It is proved that the FeCo double site successfully reduced the electrical conductivity of the electrode, which was beneficial to the electrical analysis and detection. Then, the SPCE electrodes modified with FeN<sub>4</sub>-Gra (Fig. 3a), CoN<sub>4</sub>-Gra (Fig. 3b), and FeCoN<sub>6</sub>-Gra (Fig. 3c) were successively used to detect a series of concentration gradients of As(III) by square-wave anodic dissolution voltammetry (SWASV) under optimal experimental conditions (Fig. S13). We collected three sets of current data on different electrodes modified by FeN<sub>4</sub>-Gra, CoN<sub>4</sub>-Gra, and FeCoN<sub>6</sub>-Gra to get the error bar and average value. And the calculated mean value is further fitted linearly with the concentration. Based on the active area calculated from Fig. S14, their corresponding

sensitivities were  $0.11$ ,  $0.15$ , and  $0.38 \text{ mA}\cdot\text{cm}^{-2}\cdot\text{ppb}^{-1}$ , respectively. For more intuition, Fig. 3d shows the comparison of the catalytic performance of the three electrodes. Clearly, the diatomic FeCoN<sub>6</sub>-Gra had a unique sensitivity and a satisfactory LOD ( $0.02 \text{ ppb}$ ). And the LOD is calculated using the  $3\sigma$  method, i.e.,  $3 \text{ SD}/S$ , where SD (root-mean-square deviation) and S represent standard deviation of the measurements and the slope of the calibration line, respectively [10]. Thus, the lower LOD also indicates that the FeCoN<sub>6</sub>-Gra modified electrode has better reproducibility on the electrode signal. To better directly compare the contribution of metal sites to catalyze As(III), the response signals of FeCoN<sub>6</sub>-Gra, FeN<sub>4</sub>-Gra, and CoN<sub>4</sub>-Gra catalysts were normalized by their respective metal loads. The performance results were shown in Fig. S15. FeCoN<sub>6</sub>-Gra had the best catalytic performance ( $6.14 \text{ mA}\cdot\text{mg}^{-1}\cdot\text{ppb}^{-1}$ ), and its sensitivity was more than 3 times that of homologous single atom catalyst. It was further revealed that this FeCo combination was not a simple “1 + 1” contribution pattern between Fe and Co atoms in the electrocatalytic capacity of reducing As(III). Then, the analytical performance of FeCoN<sub>6</sub>-Gra and other traditional catalytic modified electrochemical sensors reported so far is compared in Table S4. It can be seen that the hetero-diatomic FeCoN<sub>6</sub>-Gra with electron redistribution has the most outstanding sensitivity and stability, as well as LOD, indicating that the regulation of coordination structure is one of the effective ways to achieve high efficiency catalysis of As(III). In addition, FeCoN<sub>6</sub>-Gra/SPCE was used to detect other common heavy metal ions in water to better highlight its specific detection ability. As shown in Fig. S16, a series of SWASV responses were obtained near  $-1.13 \text{ V}$  (Cd (II)),  $-0.75 \text{ V}$  (Pb(II)), and  $-0.05 \text{ V}$  (Hg (II)), respectively. And the corresponding sensitivities were  $0.61$ ,  $0.90$ , and  $2.23 \mu\text{A}\cdot\text{cm}^{-2}\cdot\text{ppb}^{-1}$  [55]. On the one hand, it was clear that FeCoN<sub>6</sub>-Gra/SPCE had the highest sensitivity to As(III), even by two orders of magnitude, and had an absolute advantage in selective detection. On the other hand, it was worth mentioning that the response position of FeCoN<sub>6</sub>-Gra/SPCE to Cu(II) was near  $-0.35 \text{ V}$ , which was very close to that of As(III), indicating that the two were likely to interfere with each other (this will be discussed later).

### 3.4. Evaluation on practicability of the electrode

The stability and reproducibility of the SPCE electrode modified by FeCoN<sub>6</sub>-Gra are crucial indexes to evaluate the practical application value of the device. We performed ten repetitions of As(III) with one electrode under optimal conditions, as shown in Fig. 4a. Fig. 4b shows the test of 10 different SPCE electrodes modified with FeCoN<sub>6</sub>-Gra against  $0.3 \text{ ppb}$  concentration of As(III). The relative standard deviations (RSD) of the cumulative peak current signal were  $0.65\%$  and  $2.66\%$ , respectively, indicating that the electrode had good stability and reproducibility [56]. The anti-interference ability was also an important indicator that cannot be ignored. In a sense, it represented the accuracy of the detection data. The above experimental phenomenon (Fig. S16) showed that the signals of As(III) and Cu(II) may overlap, so it was necessary to further verify the reliability of the experimental signal. Therefore, we used the sensor to collect a series of SWASV signals of  $0.3 \text{ ppb}$  As(III) when continuously increasing the concentration of Cu(II). Satisfactorily, no stripping peak belonging to Cu(II) was found on the signal curve in Fig. 4c. When the concentration of Cu(II) is 100 times more than that of As(III), the peak current of As(III) is only increased by  $9.6\%$ . Although there is no unified standard to define the anti-interference degree of electrochemical sensors, the reported researches have shown that the peak value fluctuation within  $10.0\%$  is considered to have a good anti-interference ability when the concentration of interfering ions is 100 times higher than the target analyte [57, 58]. Based on this, it can be concluded that electrode modified by FeCoN<sub>6</sub>-Gra had the good anti-interference ability to Cu(II). Finally, the FeCoN<sub>6</sub>-Gra/SPCE was studied in a mixed solution with a ratio of  $1:9$  of actual water to buffer solution (Fig. 4d, water sample was taken from Dongpu Reservoir in Hefei, China). The electrode's sensitivity was

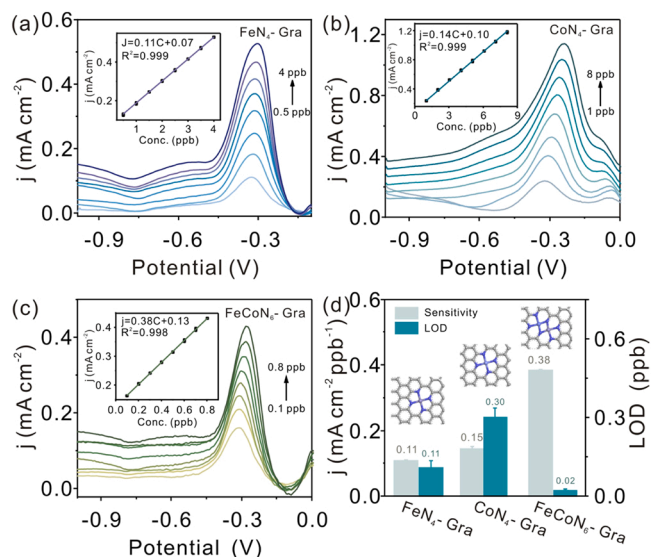


**Fig. 3.** SWASV responses of As(III) detection on the electrodes modified with (a) FeN<sub>4</sub>-Gra, (b) CoN<sub>4</sub>-Gra, and (c) FeCoN<sub>6</sub>-Gra. And the inset is corresponding linear equations. (d) Histogram comparison of the sensitivity and LOD of FeN<sub>4</sub>-Gra, CoN<sub>4</sub>-Gra, and FeCoN<sub>6</sub>-Gra (the inset is corresponding atomic structure model).

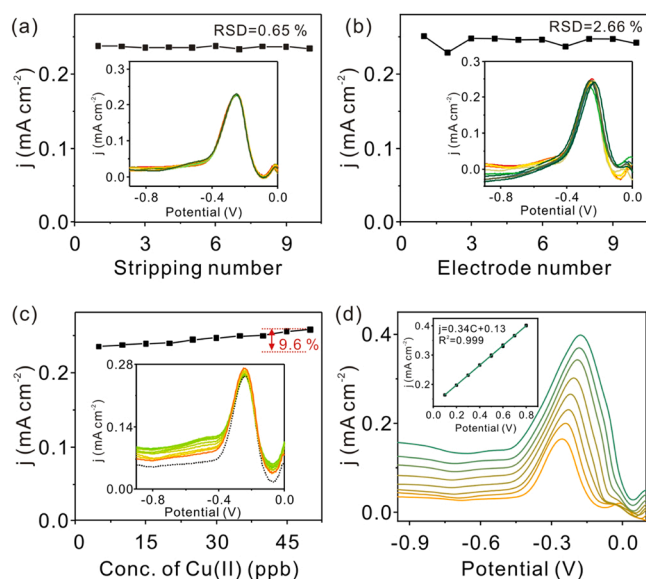


**Fig. 4.** (a) Stability experiment of 10 tests on the electrode modified with FeCoN<sub>6</sub>-Gra. (b) Reproducibility test of 10 different electrodes for the same concentration (0.3 ppb) of As(III). (c) Anti-interference signals of 0.3 ppb As(III) detected by FeCoN<sub>6</sub>-Gra in the coexistence of 5 ~ 50 ppb Cu(II). The insets are their real-time SWASV signal curves. (d) Electrochemical detection of As(III) by FeCoN<sub>6</sub>-Gra modified SPCE electrode in an electrolyte with a 9:1 ratio of acetic acid-sodium acetate buffer solution to the actual water sample. The inset is the corresponding current-concentration linear equation.

0.34 mA·cm<sup>-2</sup>·ppb<sup>-1</sup> in the range of 0.1 ~ 0.8 ppb, and the linear correlation was good. In summary, FeCoN<sub>6</sub>-Gra modified sensor had good practical application potential.

### 3.5. The chemical interaction between catalysts and As(III)

To get a clearer understanding of the interaction mechanism between the samples and As(III), the catalysts after adsorption (FeN<sub>4</sub>-Gra/As, CoN<sub>4</sub>-Gra/As, and FeCoN<sub>6</sub>-Gra/As) were subjected to XAFS analysis. By comparing the normalized XANES spectra of the K-edge of Fe/Co before and after adsorption, it can be seen that the valence state of each metal center increased to a certain extent, resulting from losing electrons. Another point worth noting was that Fe/Co in FeCoN<sub>6</sub>-Gra/As loses fewer electrons than CoN<sub>4</sub>-Gra/As or FeN<sub>4</sub>-Gra/As, which can be verified by the change of valence states in Fig. 5a and Fig. 5b. The results demonstrated that the prepared catalysts had the certain catalytic capacity to reduce As(III), but the single metal center site lost more electrons. Generally speaking, the ability to lose electrons directly evaluates the reduction ability of the catalyst. But surprisingly, the catalytic performance of FeN<sub>4</sub>-Gra and CoN<sub>4</sub>-Gra was weaker than FeCoN<sub>6</sub>-Gra. Therefore, we speculated that the number of electrons obtained by the diatomic FeCo center itself was greater than its own output, so there was no noticeable increase in the valence state, while the single-atom catalysts donated all their own electrons. To verify this, XPS analysis was performed on the adsorbed samples. From the high-resolution XPS spectrum of As 3d in Fig. 5c, the binding energy of As in FeCoN<sub>6</sub>-Gra/As was the lowest, indicating that the obtained electrons were the most [21]. At the same time, the variation trend of valence states of Fe 2p and Co 2p in Fig. 5d was consistent with the conclusion of XANES spectrum. The valence states of Fe and Co in FeCoN<sub>6</sub>-Gra were higher than that of homologous SACs after adsorption, but more electrons were lost during the adsorption and reduction process. Besides, the As-O bond in FeCoN<sub>6</sub>-Gra/As was observed to be elongated from Fig. 5e, which again confirmed the bimetallic site was the electron donor, and its unique coordination structure was more conducive to the reduction of As(III). Then we further analyzed the bonding information of metal active sites

with As species. Fig. 5f showed the fitting results of the Fe K-edge FT spectrum for FeN<sub>4</sub>-Gra/As. It can be seen that there were two scattering peaks at 1.4 and 2.1 Å assigned to Fe-N and Fe-As paths, respectively. And there were two paths corresponding to Co-N and Co-As in the K-edge FT spectrum of Co (Fig. 5g). The fitting results (Table S2) showed that the bond lengths of Fe-N and Co-N were elongated after adsorption, which revealed the fact of Fe/Co bonding with As. For FeCoN<sub>6</sub>-Gra/As, the K-edge FT spectrum of Fe was assigned with three scattering paths Fe-N, Fe-Co, and Fe-As, respectively. Within the error range, the coordination number of Fe-N and Fe-Co did not change much compared with FeCoN<sub>6</sub>-Gra. This indicated that it was the Fe atom that interacted with As(III) and carried out electron transfer through coordination with As among the diatomic sites. Satisfactorily, the fitting results in Fig. 5i did not find the path of Co-As, and the bond length of Co-Fe was consistent with that of Fe-Co in Fig. 5h. The corresponding  $k^3\chi(k)$  oscillation curve fitting of FeN<sub>4</sub>-Gra/As, CoN<sub>4</sub>-Gra/As, and FeCoN<sub>6</sub>-Gra/As in Fig. S17 perfectly proved the reliability of the data and concluded that Fe atom was the active site that really interacted with As atom.

### 3.6. Exploration of the catalytic path of As(III) from the DFT

Although very few in-situ characterizations greatly investigated some dynamic information of chemical changes during the transient electrochemical progress, the morphological changes of intermediates are still difficult to characterize or even capture. Hence, we performed DFT calculations and established relevant models based on the EXAFS fitting results to gain further insight into the catalytic mechanism of the active sites in FeN<sub>4</sub>-Gra, CoN<sub>4</sub>-Gra, and FeCoN<sub>6</sub>-Gra. Fig. 6a showed the calculated free energy diagram, which included the formation of \*H<sub>3</sub>AsO<sub>3</sub>, \*H<sub>2</sub>AsO<sub>2</sub>, \*HAsO, and \*As intermediates [10,22,59]. The illustration was the side view of the As(III) model adsorbed on FeCoN<sub>6</sub>-Gra, and the top view of the corresponding adsorption model in the stepwise reduction step was shown in Fig. S18. Throughout the whole reduction process, it can be observed that the reduction paths of FeN<sub>4</sub>-Gra and FeCoN<sub>6</sub>-Gra were both downhill, which was more favorable for the reaction from the perspective of thermodynamics. However, the energy barrier of 0.35 eV should be overcome to complete the adsorption of \*HAsO on CoN<sub>4</sub>-Gra, indicating that the bonding ability between Co and \*H<sub>2</sub>AsO<sub>2</sub> was too strong. This was not conducive to the desorption of As species from the active site, thus showing weak sensitivity in catalytic performance. In detail, both FeN<sub>4</sub>-Gra and CoN<sub>4</sub>-Gra showed relatively weak adsorption of As(III) in the first step, but FeCoN<sub>6</sub>-Gra had obvious advantages in the adsorption of H<sub>3</sub>AsO<sub>3</sub>. As shown in Fig. 6a, the adsorption mode of H<sub>3</sub>AsO<sub>3</sub> on FeCoN<sub>6</sub>-Gra was optimized into two-site adsorption (both H and As atoms were adsorbed), which was quite different from FeN<sub>4</sub>-Gra and CoN<sub>4</sub>-Gra. Further from the charge density difference image in Fig. 5b, Co transferred 0.08 e to \*OH. In addition, the combined DFT and EXAFS data found that the distance between Fe and Co was lengthened. The above findings jointly proved that the d<sub>Fe-Co</sub> (distance between Fe and Co) in adjacent double sites could match the size of the adsorbed H<sub>3</sub>AsO<sub>3</sub>, which contributed to electron transfer and thus promoting the reduction of H<sub>3</sub>AsO<sub>3</sub>. Moreover, the bond length of Fe-As bond is 2.42 Å which the distance between Co and As atom is 3.51 Å. The distance between Co and As atom is much larger than the sum of the radius of the two atoms. Therefore, Co is not sufficient to bonds with As atom. To further reveal the nature of the superior adsorption performance of FeCoN<sub>6</sub>-Gra, the interaction between As(III) and the metal center was analyzed from the point of view of DOS. Fig. 6c ~ 6e are the DOS comparison of \*HAsO adsorb on FeCoN<sub>6</sub>-Gra, FeN<sub>4</sub>-Gra, and CoN<sub>4</sub>-Gra, respectively. In the FeCoN<sub>6</sub>-Gra model, the p orbital of the O atom split around -5 eV, which was well matched with the s orbital electrons of the N atom within the range of -9.0 ~ -3.5 eV (yellow area). It further indicated that the O atom in \*HAsO interacted with the coordinated N atom. The electrons of As atom were simultaneously rearranged and highly matched with the Fe/Co atom from -6.0-0 eV (blue-filled area), demonstrating the existence of



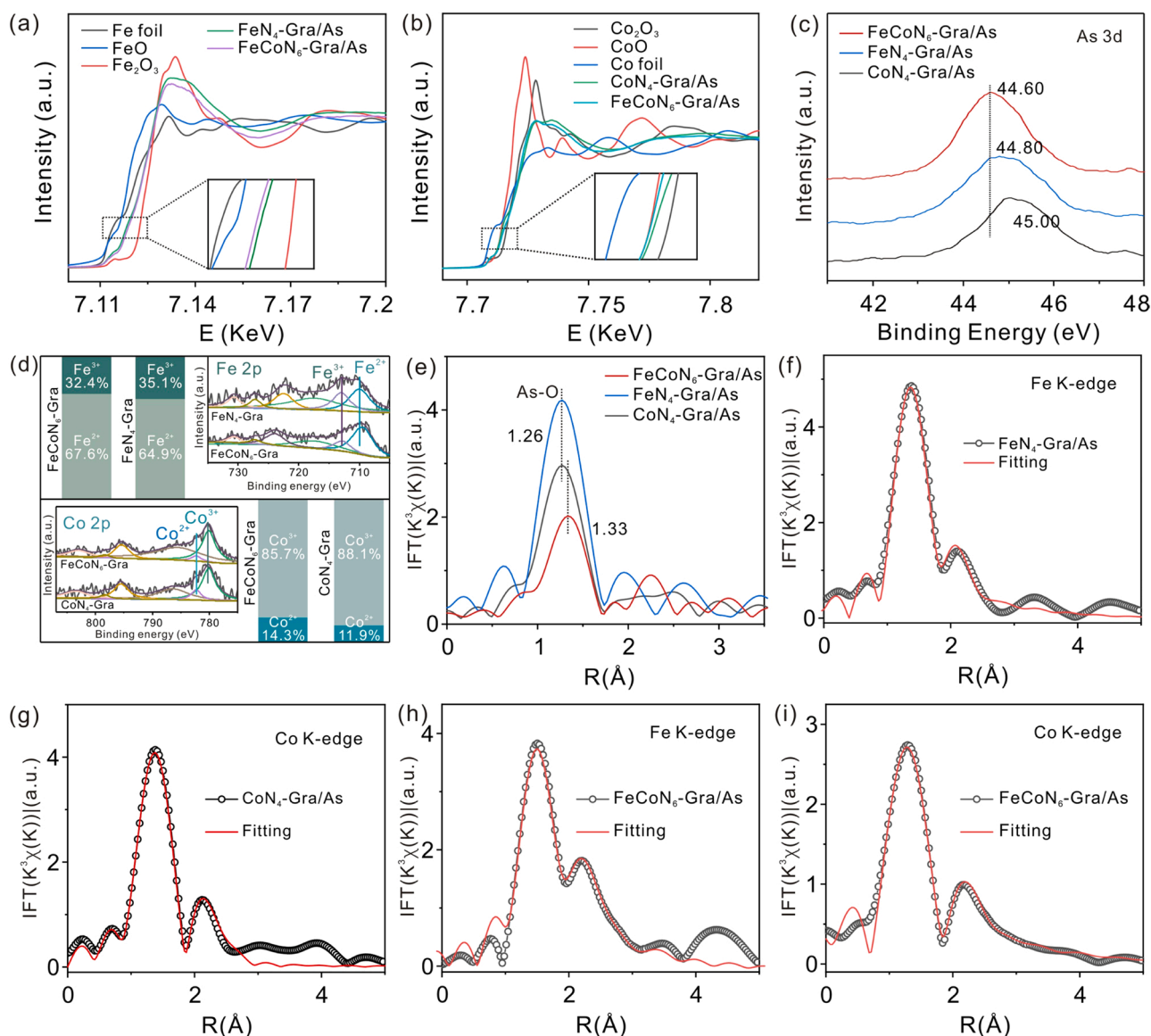


**Fig. 5.** Normalized XANES spectra of (a) Fe K-edge of the Fe foil, FeO, Fe<sub>2</sub>O<sub>3</sub>, FeN<sub>4</sub>-Gra/As, and FeCoN<sub>6</sub>-Gra/As and (b) Co K-edge XANES spectra of the Co foil, CoO, Co<sub>2</sub>O<sub>3</sub>, CoN<sub>4</sub>-Gra/As, and FeCoN<sub>6</sub>-Gra/As. The illustrations in (a) and (b) are the enlarged dashed box areas. (c) Comparison of As 3d of FeN<sub>4</sub>-Gra/As, CoN<sub>4</sub>-Gra/As and FeCoN<sub>6</sub>-Gra/As. (d) The upper half is the Fe 2p of FeN<sub>4</sub>-Gra/As and FeCoN<sub>6</sub>-Gra/As and the corresponding ratios of Fe(II) and Fe(III), the lower part is the high-resolution XPS of Co 2p in CoN<sub>4</sub>-Gra/As and FeCoN<sub>6</sub>-Gra/As and their corresponding Co(II) and Co(III) proportions. (e) As K-edge EXAFS FT spectra of FeN<sub>4</sub>-Gra/As, CoN<sub>4</sub>-Gra/As, and FeCoN<sub>6</sub>-Gra/As without correcting for scattering phase shift ( $k^3$ -weighted). (f) Fe K-edge EXAFS FT spectra of FeN<sub>4</sub>-Gra/As and (g) Co K-edge EXAFS FT spectra of CoN<sub>4</sub>-Gra/As ( $k^3$ -weighted) and their corresponding fitting curves. (h) Fe K-edge and (i) Co K-edge EXAFS FT spectra of FeCoN<sub>6</sub>-Gra/As ( $k^3$ -weighted) and their corresponding fitting curves.

strong electron coupling between As atom and the Fe atom based on the optimized model structure. Most importantly, the As species showed dynamic migration from Fe to Co site during the entire reduction route. The bond length of Fe-As showed a law of first decreasing and then increasing (parameters were listed in Table S5), corresponding to the shortest bond length of 2.26 Å in the ring-determining step. On the one hand, it showed that the existence of the neighboring Co atom induced the electron distribution of Fe atoms to disperse and matched with the As energy level, which further caused the electron rearrangement of O atom and electron transferred with the coordination N atom. On the other hand, Co atoms could drive the migration of the As species to bridge sites between FeCo, which was conducive to the fracture of As-O bond, resulting in the efficient catalysis of the diatomic model. Furthermore, the large bond length means that the bond between the intermediate with the metal active site is more likely to break the bond, which benefits to the following dissociation process. Moreover, the bond

population of FeCoN<sub>6</sub>-Gra also shows a similar rule with bond length (Table S5). It means that the two-site interaction is more conducive to the dissociation process, thus effectively avoiding the inactivation of the active site. A comprehensive observation of Fig. 6d and Fig. 6e showed that the DOS of *p* orbitals of O atoms did not change much (dashed line at -4 eV). The electron distribution of Fe/Co atoms was relatively local, matching the energy level of As atom in the range of -3 ~ 0 eV (blue area). It was worth emphasizing that Fe atom fit better. However, there was a certain electron coupling between the H atom and the N atom in FeN<sub>4</sub>-Gra, indicating that HAsO contributed to the fracture of As-O through the coordination of the Fe and H atom, which was not found in CoN<sub>4</sub>-Gra. Unfortunately, the bond length of Fe-As in FeN<sub>4</sub>-Gra was usually very short, resulting in difficulty in desorption intermediates and inactivation of catalyst sites.

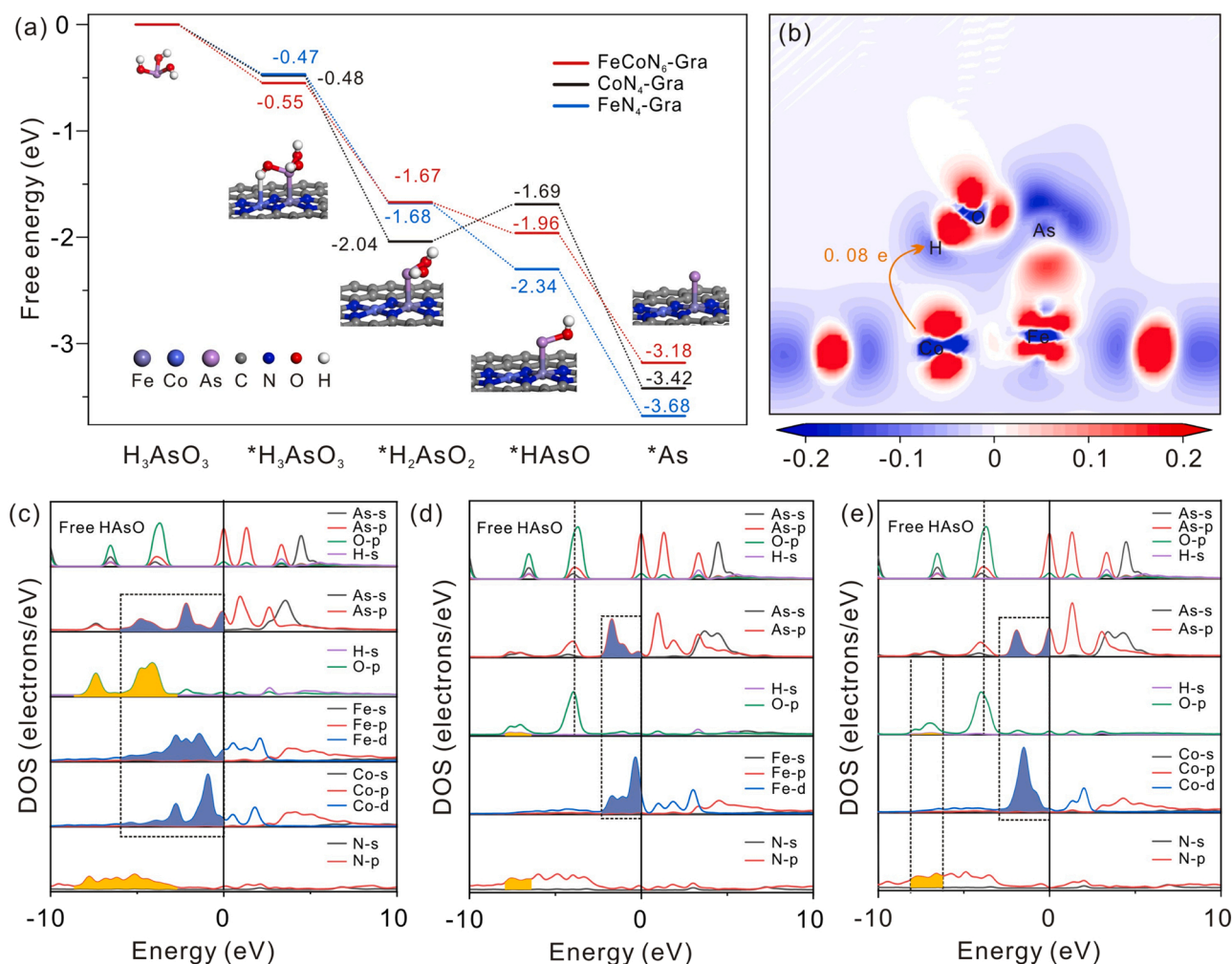


**Fig. 6.** (a) Comparison of DFT calculations for  $\text{H}_3\text{AsO}_3$  dissociation paths on  $\text{FeN}_4\text{-Gra}$ ,  $\text{CoN}_4\text{-Gra}$ , and  $\text{FeCoN}_6\text{-Gra}$ , respectively. The asterisk (\*) represents species located at active metal sites. (b) Charge density difference image of  $\text{H}_3\text{AsO}_3$  adsorbed on  $\text{FeCoN}_6\text{-Gra}$ . The blue area represented the loss of electrons, red represented electron accumulation. The DOS comparison of  $^*\text{HAsO}$  adsorbed on (c)  $\text{FeCoN}_6\text{-Gra}$ , (d)  $\text{FeN}_4\text{-Gra}$ , and (e)  $\text{CoN}_4\text{-Gra}$ , respectively.

#### 4. Conclusion

In this work, a highly efficient electrocatalyst composed of heteronuclear  $\text{FeCo}$  diatoms was constructed as the sensitive probe, which improved the electrochemical performance of  $\text{As(III)}$ . DFT calculation and experimental analysis showed that the adjacent  $\text{CoN}_4$  in  $\text{FeCoN}_6\text{-Gra}$  created a new electron arrangement to the metal pair center, emphasizing the influence of the two-site adsorption mode of the atomic pair on promoting electron transfer on the surface. Meanwhile, the neighboring  $\text{CoN}_4$  together with the  $\text{FeN}_4$  group pull the  $\text{As}$  species toward the bridge site of the atomic pair, thereby promoting the reduction of  $\text{As(III)}$  by accelerating the  $\text{As-O}$  bond breaking. This work not only contributes to the realization of highly active and selective electrocatalytic reduction of  $\text{As(III)}$ , but more importantly contribute to a better understanding of the intrinsic activity enhancement of diatomic catalysts.

#### CRediT authorship contribution statement

**Yong-Yu Li:** Conceptualization, Investigation, Validation, Formal analysis, Methodology, Writing – original draft. **Zong-Yin Song:** Validation, Software. **Zhi-Wei Gao:** Writing – review & editing. **Xiang-Yu Xiao:** Formal analysis, Writing – review & editing. **Yong-Huan Zhao:** Writing – review & editing. **Pei-Hua Li:** Project administration, Supervision, Funding acquisition. **Xing-Jiu Huang:** Project administration, Supervision, Funding acquisition, Resources Writing – review & editing.

**Wen-Qing Liu:** Conceptualization, Funding acquisition, Resources.

#### Declaration of Competing Interest

The authors declare that they have no known competing financial interests or personal relationships that could have appeared to influence the work reported in this paper.

#### Data Availability

The data that has been used is confidential.

#### Acknowledgements

This work was supported by the Project of the National Key R&D Program of China (2021YFB3201400), the Key R&D Program of Anhui Province (202104i07020006, 202104i07020011), the National Natural Science Foundation of China (22206187), the China Postdoctoral Innovation Talents Supporting Project (BX2021317), Anhui Provincial Natural Science Foundation (2208085QB57), the HFIPS Director's Fund (YZJJ2022QN26, YZJJ202302-TS), the Open Funds of the State Key Laboratory of Electronanalytical Chemistry (SKLEAC202312) and Special Foundation of President of the Chinese Academy of Sciences. Thanks to Ms. Zong-Yin Song for her important contribution in the DFT calculations of this work.



## Appendix A. Supporting information

Supplementary data associated with this article can be found in the online version at [doi:10.1016/j.apcatb.2023.122851](https://doi.org/10.1016/j.apcatb.2023.122851).

## References

- [1] M.F. Hughes, Arsenic toxicity and potential mechanisms of action, *Toxicol. Lett.* 133 (2002) 1–16, [https://doi.org/10.1016/S0378-4274\(02\)00084-x](https://doi.org/10.1016/S0378-4274(02)00084-x).
- [2] V.K. Sharma, M. Sohn, Aquatic arsenic: toxicity, speciation, transformations, and remediation, *Environ. Int.* 35 (2009) 743–759, <https://doi.org/10.1016/j.envint.2009.01.005>.
- [3] D.K. Nordstrom, Worldwide occurrences of arsenic in ground water, *Science* 296 (2002) 2143, <https://doi.org/10.1126/science.1072375>.
- [4] M.B. Joel Podgorski, Global threat of arsenic in groundwater, *Science* 368 (2020) 845–850, <https://doi.org/10.1126/science.aba1510>.
- [5] J. Wang, J. Liu, X. Peng, M. He, X. Hu, J. Zhao, F. Zhu, X. Yang, L. Kong, Reductive removal of As(V) and As(III) from aqueous solution by the UV/sulfite process: recovery of elemental arsenic, *Water Res.* 223 (2022), 118981, <https://doi.org/10.1016/j.watres.2022.118981>.
- [6] X.Y. Xiao, Y.H. Zhao, Y.Y. Li, Z.Y. Song, S.H. Chen, H.Q. Huang, M. Yang, P.H. Li, X.J. Huang, General strategies to construct highly efficient sensing interfaces for metal ions detection from the perspective of catalysis, *Anal. Chem.* 94 (2022) 13631–13641, <https://doi.org/10.1021/acs.analchem.2c01797>.
- [7] Y. Guo, B. Dai, J. Peng, C. Wu, Y. Xie, Electron transport in low dimensional solids: a surface chemistry perspective, *J. Am. Chem. Soc.* 141 (2019) 723–732, <https://doi.org/10.1021/jacs.8b09821>.
- [8] S.S. Li, W.Y. Zhou, M. Jiang, Z. Guo, J.H. Liu, L. Zhang, X.J. Huang, Surface Fe(II)/Fe(III) cycle promoted ultra-highly sensitive electrochemical sensing of arsenic(III) with dumbbell-like Au/Fe<sub>3</sub>O<sub>4</sub> nanoparticles, *Anal. Chem.* 90 (2018) 4569–4577, <https://doi.org/10.1021/acs.analchem.7b04981>.
- [9] S.H. Chen, Z.Y. Song, X.Y. Xiao, H.Q. Huang, Y.F. Yang, P.H. Li, M. Yang, X. J. Huang, Engineering electron-rich sites on CoSe<sub>2-x</sub> nanosheets for the enhanced electroanalysis of As(III): a study on the electronic structure via X-ray absorption fine structure spectroscopy and density functional theory calculation, *Anal. Chem.* 94 (2022) 3211–3218, <https://doi.org/10.1021/acs.analchem.1c04785>.
- [10] P.H. Li, Z.Y. Song, X.Y. Xiao, B. Liang, M. Yang, S.H. Chen, W.Q. Liu, X.J. Huang, Coordination engineering strategy of iron single-atom catalysts boosts anti-Cu(II) interference detection of As(III) with a high sensitivity, *J. Hazard. Mater.* 442 (2023), 130122, <https://doi.org/10.1016/j.jhazmat.2022.130122>.
- [11] W. Qu, H. Yuan, Z. Ren, J. Qi, D. Xu, J. Chen, L. Chen, H. Yang, Z. Ma, X. Liu, H. Wang, X. Tang, An atom-pair design strategy for optimizing the synergistic electron effects of catalytic sites in NO selective reduction, *Angew. Chem. Int. Ed. Engl.* (2022), e202212703, <https://doi.org/10.1002/anie.202212703>.
- [12] S. Schauermaann, J. Hoffmann, V. Johánek, J. Hartmann, J. Libuda, H.-J. Freund, Catalytic activity and poisoning of specific sites on supported metal nanoparticles, *Angew. Chem. Int. Ed.* 41 (2002) 2532–2535, [https://doi.org/10.1002/1521-3773\(20020715\)41:14<2532::Aid-anie2532>3.0.Co;2-3](https://doi.org/10.1002/1521-3773(20020715)41:14<2532::Aid-anie2532>3.0.Co;2-3).
- [13] K. Qi, M. Chhowalla, D. Voiry, Single atom is not alone: metal-support interactions in single-atom catalysis, *Mater. Today* 40 (2020) 173–192, <https://doi.org/10.1016/j.mattod.2020.07.002>.
- [14] R. Zhao, J. Chen, Z. Chen, X. Jiang, G. Fu, Y. Tang, W. Jin, J.-M. Lee, S. Huang, Atomically dispersed CoN<sub>4</sub>/B, N-C nanotubes boost oxygen reduction in rechargeable Zn-Air batteries, *ACS Appl. Energy Mater.* 3 (2020) 4539–4548, <https://doi.org/10.1021/acsaelm.0c00215>.
- [15] J. Chen, H. Li, C. Fan, Q. Meng, Y. Tang, X. Qiu, G. Fu, T. Ma, Dual single-atomic Ni-N<sub>4</sub> and Fe-N<sub>4</sub> sites constructing janus hollow graphene for selective oxygen electrocatalysis, *Adv. Mater.* 32 (2020), e2003134, <https://doi.org/10.1002/adma.202003134>.
- [16] C. Fan, X. Wang, X. Wu, Y. Chen, Z. Wang, M. Li, D. Sun, Y. Tang, G. Fu, Neodymium-evoked valence electronic modulation to balance reversible oxygen electrocatalysis, *Adv. Energy Mater.* 13 (2022), <https://doi.org/10.1002/aenm.202203244>.
- [17] Z. Jin, M. Yang, S.H. Chen, J.H. Liu, Q.X. Li, X.J. Huang, Tin oxide crystals exposed by low-energy {110} facets for enhanced electrochemical heavy metal ions sensing: X-ray absorption fine structure experimental combined with density-functional theory evidence, *Anal. Chem.* 89 (2017) 2613–2621, <https://doi.org/10.1021/acs.analchem.6b04977>.
- [18] W.Y. Zhou, J.Y. Liu, J.Y. Song, J.J. Li, J.H. Liu, X.J. Huang, Surface-electronic-state-modulated, single-crystalline (001) TiO<sub>2</sub> nanosheets for sensitive electrochemical sensing of heavy-metal ions, *Anal. Chem.* 89 (2017) 3386–3394, <https://doi.org/10.1021/acs.analchem.6b04023>.
- [19] H. Fei, J. Dong, D. Chen, T. Hu, X. Duan, I. Shakir, Y. Huang, X. Duan, Single atom electrocatalysts supported on graphene or graphene-like carbons, *Chem. Soc. Rev.* 48 (2019) 5207–5241, <https://doi.org/10.1039/c9cs00422j>.
- [20] S.K. Kaiser, Z. Chen, D. Faust Akl, S. Mitchell, J. Perez-Ramirez, Single-atom catalysts across the periodic table, *Chem. Rev.* 120 (2020) 11703–11809, <https://doi.org/10.1021/acs.chemrev.0c00576>.
- [21] Z.Y. Song, X.Y. Xiao, S.H. Chen, Y.Y. Li, Y.F. Yang, C.C. Huang, W. Duan, M. Yang, P.H. Li, X.J. Huang, Sensing material-dependent interference of multiple heavy metal ions: experimental and simulated thermodynamics study on Cu(II), Cd(II), and As(III) electroanalysis, *Anal. Chem.* 94 (2022) 6225–6233, <https://doi.org/10.1021/acs.analchem.1c05617>.
- [22] Z.Y. Song, Z.W. Gao, Y.Y. Li, W. Duan, X.Y. Xiao, Y.H. Zhao, Y.F. Yang, C.C. Huang, M. Yang, S.H. Chen, P.H. Li, X.J. Huang, Generalizable descriptors of highly sensitive detection of As(III) over transition-metal single atoms: a combined density function theory and gradient boosting regression approach, *Anal. Chem.* 95 (2023) 3666–3674, <https://doi.org/10.1021/acs.analchem.2c04617>.
- [23] A. Bhardwaj, J. Kaur, M. Wuest, F. Wuest, In situ click chemistry generation of cyclooxygenase-2 inhibitors, *Nat. Commun.* 8 (2017) 1, <https://doi.org/10.1038/s41467-016-0009-6>.
- [24] H. Zhang, X. Jin, J.M. Lee, X. Wang, Tailoring of active sites from single to dual atom sites for highly efficient electrocatalysis, *ACS Nano* 16 (2022) 17572–17592, <https://doi.org/10.1021/acsnano.2c06827>.
- [25] X. Liang, N. Fu, S. Yao, Z. Li, Y. Li, The progress and outlook of metal single-atom-site catalysis, *J. Am. Chem. Soc.* 144 (2022) 18155–18174, <https://doi.org/10.1021/jacs.1c12642>.
- [26] T. Tang, Z. Wang, J. Guan, Optimizing the electrocatalytic selectivity of carbon dioxide reduction reaction by regulating the electronic structure of single-atom M-N-C materials, *Adv. Funct. Mater.* 32 (2022), 2111504, <https://doi.org/10.1002/adfm.202111504>.
- [27] M. Ma, A. Kumar, D. Wang, Y. Wang, Y. Jia, Y. Zhang, G. Zhang, Z. Yan, X. Sun, Boosting the bifunctional oxygen electrocatalytic performance of atomically dispersed Fe site via atomic Ni neighboring, *Appl. Catal. B-Environ.* 274 (2020), 119091, <https://doi.org/10.1016/j.apcatb.2020.119091>.
- [28] J. Wang, W. Liu, G. Luo, Z. Li, C. Zhao, H. Zhang, M. Zhu, Q. Xu, X. Wang, C. Zhao, Y. Qu, Z. Yang, T. Yao, Y. Li, Y. Lin, Y. Wu, Y. Li, Synergistic effect of well-defined dual sites boosting the oxygen reduction reaction, *Energ. Environ. Sci.* 11 (2018) 3375–3379, <https://doi.org/10.1039/c8ee02656d>.
- [29] M. Xiao, Y. Chen, J. Zhu, H. Zhang, X. Zhao, L. Gao, X. Wang, J. Zhao, J. Ge, Z. Jiang, S. Chen, C. Liu, W. Xing, Climbing the apex of the ORR volcano plot via binuclear site construction: electronic and geometric engineering, *J. Am. Chem. Soc.* 141 (2019) 17763–17770, <https://doi.org/10.1021/jacs.9b08362>.
- [30] L. Tao, Y. Wang, Y. Zou, N. Zhang, Y. Zhang, Y. Wu, Y. Wang, R. Chen, S. Wang, Charge transfer modulated activity of carbon-based electrocatalysts, *Adv. Energy Mater.* 10 (2019), <https://doi.org/10.1002/aenm.201901227>.
- [31] S. Dou, J. Song, S. Xi, Y. Du, J. Wang, Z.F. Huang, Z.J. Xu, X. Wang, Boosting electrochemical CO<sub>2</sub> reduction on metal-organic frameworks via ligand doping, *Angew. Chem. Int. Ed. Engl.* 58 (2019) 4041–4045, <https://doi.org/10.1002/anie.201814711>.
- [32] J. Wang, Structural tuning of heterogeneous molecular catalysts for electrochemical energy conversion, *Sci. Adv.* 7 (2021), eabf3989.
- [33] J. Leverett, R. Daiyan, L. Gong, K. Iputera, Z. Tong, J. Qu, Z. Ma, Q. Zhang, S. Cheong, J. Cairney, R.S. Liu, X. Lu, Z. Xia, L. Dai, R. Amal, Designing undercoordinated Ni-N<sub>x</sub> and Fe-N<sub>x</sub> on holey graphene for electrochemical CO<sub>2</sub> conversion to syngas, *ACS Nano* 15 (2021) 12006–12018, <https://doi.org/10.1021/acsnano.1c03293>.
- [34] Y. Li, B. Wei, M. Zhu, J. Chen, Q. Jiang, B. Yang, Y. Hou, L. Lei, Z. Li, R. Zhang, Y. Lu, Synergistic effect of atomically dispersed Ni-Zn pair sites for enhanced CO<sub>2</sub> electroreduction, *Adv. Mater.* 33 (2021), e2102212, <https://doi.org/10.1002/adma.202102212>.
- [35] W. Ren, X. Tan, W. Yang, C. Jia, S. Xu, K. Wang, S.C. Smith, C. Zhao, Isolated diatomic Ni-Fe metal-nitrogen sites for synergistic electroreduction of CO<sub>2</sub>, *Angew. Chem. Int. Ed. Engl.* 58 (2019) 6972–6976, <https://doi.org/10.1002/anie.201901575>.
- [36] T. Cui, Y.P. Wang, T. Ye, J. Wu, Z. Chen, J. Li, Y. Lei, D. Wang, Y. Li, Engineering dual single-atom sites on 2D ultrathin N-doped carbon nanosheets attaining ultra-low-temperature zinc-air battery, *Angew. Chem. Int. Ed. Engl.* 61 (2022), e202115219, <https://doi.org/10.1002/anie.202115219>.
- [37] J. Hao, Z. Zhuang, J. Hao, C. Wang, S. Lu, F. Duan, F. Xu, M. Du, H. Zhu, Interatomic electronegativity offset dictates selectivity when catalyzing the CO<sub>2</sub> reduction reaction, *Adv. Energy Mater.* 12 (2022), 2200579, <https://doi.org/10.1002/aenm.202200579>.
- [38] D. Liu, Y. Zhao, C. Wu, W. Xu, S. Xi, M. Chen, L. Yang, Y. Zhou, Q. He, X. Li, B. Ge, L. Song, J. Jiang, Q. Yan, Triggering electronic coupling between neighboring hetero-diatom metal sites promotes hydrogen evolution reaction kinetics, *Nano Energy* 98 (2022), 107296, <https://doi.org/10.1016/j.nanoen.2022.107296>.
- [39] J.D. Yi, X. Gao, H. Zhou, W. Chen, Y. Wu, Design of Co-Cu diatomic site catalysts for high-efficiency synergistic CO<sub>2</sub> electroreduction at industrial-level current density, *Angew. Chem. Int. Ed. Engl.* 61 (2022), e202212329, <https://doi.org/10.1002/anie.202212329>.
- [40] B. Wang, C. Cheng, M. Jin, J. He, H. Zhang, W. Ren, J. Li, D. Wang, Y. Li, A site distance effect induced by reactant molecule matchup in single-atom catalysts for fenton-like reactions, *Angew. Chem. Int. Ed. Engl.* 61 (2022), e202207268, <https://doi.org/10.1002/anie.202207268>.
- [41] L. Ma, J. Qian, Y. Li, Y. Cheng, S. Wang, Z. Wang, C. Peng, K. Wu, J. Xu, I. Manke, C. Yang, P. Adelhelm, R. Chen, Binary metal single atom electrocatalysts with synergistic catalytic activity toward high-rate and high areal-capacity lithium-sulfur batteries, *Adv. Funct. Mater.* (2022), 2208666, <https://doi.org/10.1002/adfm.202208666>.
- [42] P.H. Li, M. Yang, Z.Y. Song, S.H. Chen, X.Y. Xiao, C.H. Lin, X.J. Huang, Highly sensitive and stable determination of As(III) under near-neutral conditions: benefit from the synergistic catalysis of Pt single atoms and active S atoms over Pt<sub>1</sub>/MoS<sub>2</sub>, *Anal. Chem.* 93 (2021) 15115–15123, <https://doi.org/10.1021/acs.analchem.1c03416>.
- [43] X.Y. Xiao, Z.Y. Song, P.H. Li, S.H. Chen, L.N. Li, M. Yang, C.H. Lin, X.J. Huang, Au<sub>25</sub> nanoclusters exhibit superhigh catalytic activity in electrochemical detection of As(III), *Anal. Chem.* 93 (2021) 14014–14023, <https://doi.org/10.1021/acs.analchem.1c03748>.

- [44] Y.Y. Li, Z.Y. Song, X.Y. Xiao, L.K. Zhang, H.Q. Huang, W.Q. Liu, X.J. Huang, In-situ electronic structure redistribution tuning of single-atom Mn/g-C<sub>3</sub>N<sub>4</sub> catalyst to trap atomic-scale lead(II) for highly stable and accurate electroanalysis, *J. Hazard. Mater.* 435 (2022), 129009, <https://doi.org/10.1016/j.jhazmat.2022.129009>.
- [45] Z. Chen, X. Liao, C. Sun, K. Zhao, D. Ye, J. Li, G. Wu, J. Fang, H. Zhao, J. Zhang, Enhanced performance of atomically dispersed dual-site Fe-Mn electrocatalysts through cascade reaction mechanism, *Appl. Catal. B-Environ.* 288 (2021), 120021, <https://doi.org/10.1016/j.apcatb.2021.120021>.
- [46] Z. Guo, Y. Xie, J. Xiao, Z.J. Zhao, Y. Wang, Z. Xu, Y. Zhang, L. Yin, H. Cao, J. Gong, Single-atom Mn-N<sub>4</sub> site-catalyzed peroxone reaction for the efficient production of hydroxyl radicals in an acidic solution, *J. Am. Chem. Soc.* 141 (2019) 12005–12010, <https://doi.org/10.1021/jacs.9b04569>.
- [47] H. Yang, Y. Wu, G. Li, Q. Lin, Q. Hu, Q. Zhang, J. Liu, C. He, Scalable production of efficient single-atom copper decorated carbon membranes for CO<sub>2</sub> electroreduction to methanol, *J. Am. Chem. Soc.* 141 (2019) 12717–12723, <https://doi.org/10.1021/jacs.9b04907>.
- [48] S. Huang, Z. Qiao, P. Sun, K. Qiao, K. Pei, L. Yang, H. Xu, S. Wang, Y. Huang, Y. Yan, D. Cao, The strain induced synergistic catalysis of FeN<sub>4</sub> and MnN<sub>3</sub> dual-site catalysts for oxygen reduction in proton- /anion- exchange membrane fuel cells, *Appl. Catal. B-Environ.* 317 (2022), 121770, <https://doi.org/10.1016/j.apcatb.2022.121770>.
- [49] Q. Meng, H. Hu, D. Hao, S. Yuan, J. He, X. Yu, Z. Xie, K. Wang, Y. Tang, K. Zhao, C. Xu, Application of single-atom Fe implanted N-doped carbon material as co-catalyst in the Fenton-like reaction and exploration of its enhanced activity, *J. Environ. Chem. Eng.* 10 (2022), 108843, <https://doi.org/10.1016/j.jece.2022.108843>.
- [50] P. Xia, Z. Ye, L. Zhao, Q. Xue, S. Lanzalaco, Q. He, X. Qi, I. Sirés, Tailoring single-atom FeN<sub>4</sub> moieties as a robust heterogeneous catalyst for high-performance electro-Fenton treatment of organic pollutants, *Appl. Catal. B-Environ.* 322 (2023), 122116, <https://doi.org/10.1016/j.apcatb.2022.122116>.
- [51] C. Liu, T. Li, X. Dai, J. Zhao, D. He, G. Li, B. Wang, X. Cui, Catalytic activity enhancement on alcohol dehydrogenation via directing reaction pathways from single- to double-atom catalysis, *J. Am. Chem. Soc.* 144 (2022) 4913–4924, <https://doi.org/10.1021/jacs.1c12705>.
- [52] L. Giordano, K. Akkijaru, R. Jacobs, D. Vivona, D. Morgan, Y. Shao-Horn, Electronic structure-based descriptors for oxide properties and functions, *Acc. Chem. Res.* 55 (2022) 298–308, <https://doi.org/10.1021/acs.accounts.1c00509>.
- [53] F. Li, G.F. Han, J.B. Baek, Nanocatalytic materials for energy-related small-molecules conversions: active site design, identification and structure-performance relationship discovery, *Acc. Chem. Res.* 55 (2022) 110–120, <https://doi.org/10.1021/acs.accounts.1c00645>.
- [54] H.Y. Zhuo, X. Zhang, J.X. Liang, Q. Yu, H. Xiao, J. Li, Theoretical understandings of graphene-based metal single-atom catalysts: stability and catalytic performance, *Chem. Rev.* 120 (2020) 12315–12341, <https://doi.org/10.1021/acs.chemrev.0c00818>.
- [55] S.-H. Chen, J.-J. Zhu, P.-H. Li, Y.-F. Sun, M. Yang, X.-J. Huang, In-situ growth of zero-valent iron in FeO<sub>x</sub>/Mn<sub>3</sub>O<sub>4</sub> to improve the surficial redox for high-efficient electrocatalysis of Pb(II), *Chem. Eng. J.* 430 (2022), 132959, <https://doi.org/10.1016/j.cej.2021.132959>.
- [56] X.Y. Xiao, Z.Y. Song, H. Xie, Y.H. Zhao, S.H. Chen, Y.Y. Li, M. Yang, P.H. Li, H. Ji, X.J. Huang, Unexpected redispersion effect of Au nanoclusters for enormous enhancement of electrocatalytic stability and activity, *Adv. Funct. Mater.* 32 (2022), <https://doi.org/10.1002/adfm.202209283>.
- [57] H.Q. Huang, Y.Y. Li, S.H. Chen, Z.G. Liu, Y.M. Cui, H.Q. Li, Z. Guo, X.J. Huang, Noble-metal-free Fe<sub>3</sub>O<sub>4</sub>/Co<sub>3</sub>S<sub>4</sub> nanosheets with oxygen vacancies as an efficient electrocatalyst for highly sensitive electrochemical detection of As(III), *Anal. Chim. Acta* 1189 (2022), 339208, <https://doi.org/10.1016/j.aca.2021.339208>.
- [58] C.-Y. Li, Y.-Y. Wei, W. Shen, X. Dong, M. Yang, J. Wei, Ultrahigh sensitivity electroanalysis of trace As(III) in water and human serum via gold nanoparticles uniformly anchored to Co<sub>3</sub>O<sub>4</sub> porous microspheres, *Electrochim. Acta* 368 (2021), <https://doi.org/10.1016/j.electacta.2020.137605>.
- [59] P.H. Li, M. Yang, Y.X. Li, Z.Y. Song, J.H. Liu, C.H. Lin, J. Zeng, X.J. Huang, Ultra-sensitive and selective detection of arsenic(III) via electroanalysis over cobalt single-atom catalysts, *Anal. Chem.* 92 (2020) 6128–6135, <https://doi.org/10.1021/acs.analchem.0c00677>.